How to cite: *Angew. Chem. Int. Ed.* **2025**, *64*, e202501895
doi.org/10.1002/anie.202501895

Organic Light-Emitting Diodes | Hot Paper

Pure Hydrocarbon Hosts Enabling Efficient Multi-Resonance TADF Blue-Emitting Organic Light-Emitting Diodes

Yue-Jian Yang[+], Denis Ari[+], Zhe-Hong Yu[+], Kelvine Letellier, Olivier Jeannin, Qi Zheng, Aziz Khan, Cassandre Quinton, Dong-Ying Zhou, Zuo-Quan Jiang,* and Cyril Poriel**

Abstract: Pure hydrocarbon (PHC) materials are a class of highly efficient and stable host materials for organic light-emitting diodes (OLEDs), composed solely of carbon and hydrogen atoms. Despite recent great advancements in PHC research, their applications are still mainly limited to phosphorescent OLEDs (PHOLEDs). High-performance blue OLEDs still pose a considerable challenge. Thus, expanding PHC materials into other types of OLEDs is critical for advancing organic electronic technologies. In this study, we designed a series of original high-triplet PHC materials based on a multi-substitution approach of the 9,9′-spirobifluorene (SBF) backbone and used them, for the first time, as a host in phosphorescence-sensitized multi-resonance thermally activated delayed fluorescence (MR-TADF) OLEDs. Devices based on the 2,6-bis(3,6-di-tert-butyl-9H-carbazol-9-yl)boron (DtBuCzB) emitter, using FIrpic or fac-Ir(tpz)$_3$ as the sensitizer, achieved high maximum external quantum efficiency (EQE_{max}) values ranging from 29.1 % to 33.9 %. Additionally, blue MR-TADF OLED devices based on *ν*-DABNA with a phosphorescent sensitizer (CN–Ir), demonstrated outstanding electroluminescent performance, with an EQE_{max} of approximately 31 % due to an excellent molecular orientation induced by the PHC hosts. All devices exhibited narrow full-width at half-maximum spectra and minimal efficiency roll-off. This study marks the first application of PHC materials as hosts in phosphorescence-sensitized MR-TADF OLEDs, highlighting their potential as promising candidates for next-generation blue OLEDs and offering a viable pathway to achieve high-performance devices.

Introduction

The development of organic electronics, particularly organic light-emitting diode devices (OLEDs) technology, is beginning to impact daily life significantly.[1] Based on different photophysical principles, three generations of primary luminescent materials have been developed: fluorescent materials, phosphorescent materials,[2–7] and thermally activated delayed fluorescence (TADF) materials.[8–11] Despite considerable progress in the past decades, blue light emission still needs to be improved in terms of efficiency, stability and color purity.[2,12–13] This is a major challenge for the future of lighting and display. Stability has always been an important issue in blue OLED technology, which has significantly slowed down its development and commercialization. The bond dissociation energy plays a critical role in OLED degradation, a process known as *the exciton-induced degradation process*.[14] As C–N, C–P and C–S bonds are known to be significantly more fragile than C–C bonds,[15–18] pure hydrocarbon (PHC) materials,[19] only constituted of hydrogen and carbon atoms, have appeared as a possible solution for the next generation of blue OLEDs. Removing heteroatoms from the molecular structure of host materials for phosphorescent OLEDs (PHOLEDs) not only reduces structural synthetic complexity and production costs but also simplifies technological processes, which is particularly important given the current focus on ecological transformation.[20,21]

Although the PHC strategy was introduced as early as 2005 and used in various optoelectronic fields,[22] progress has been relatively slow[23–26] and the first high-performance devices have only appeared in recent years.[27–28] Nowadays, several PHC materials have provided high-efficiency blue PHOLEDs and have even surpassed the performance of their heteroatom-based counterparts, clearly showing their real potential.[29–33] Despite these advances in OLED research using PHC host materials, the broad electroluminescent (EL) emission spectra and relatively moderate efficiency have hindered their application in display technologies. Recently, the advent of multiple resonance ther-

[*] Y.-J. Yang,[+] Z.-H. Yu,[+] Q. Zheng, A. Khan, D.-Y. Zhou, Z.-Q. Jiang
Institute of Functional Nano & Soft Materials (FUNSOM), Joint International Research Laboratory of Carbon-Based Functional Materials and Devices, Soochow University, Suzhou, 215123, Jiangsu, PR China
E-mail: zqjiang@suda.edu.cn
dyzhou@suda.edu.cn

Y.-J. Yang,[+] Z.-H. Yu,[+] Q. Zheng, A. Khan, D.-Y. Zhou, Z.-Q. Jiang
Jiangsu Key Laboratory for Carbon-Based Functional Materials & Devices, Soochow University, Suzhou, 215123, Jiangsu, PR China

D. Ari,[+] K. Letellier, O. Jeannin, C. Quinton, C. Poriel
Univ Rennes, CNRS, ISCR-UMR CNRS 6226, F-35000 Rennes
E-mail: cyril.poriel@univ-rennes.fr

[+] Equal contribution

mally activated delayed fluorescence (MR-TADF) has transformed the development of OLED materials by enabling both high color purity and high efficiency, which are essential for high-definition OLED displays.[34–36] Based on the very promising previous results obtained with PHC in PHOLEDs,[29–33] it would be highly appealing to combine novel PHC host materials with MR-TADF emitting materials through the phosphorescent sensitization technique, which has garnered significant attention for its ability to enhance efficiency and mitigate efficiency roll-off.[37–42] Although the application of PHC-based host materials in phosphorescence-sensitized devices has not yet been demonstrated, their ability to meet the practical requirements of this technology makes them worthy of exploration in this study. In Figure 1, the mechanism of PHC host-based phosphorescence-sensitized MR-TADF OLEDs is presented. The initial first 25 % singlet excited state (S_1) and first 75 % triplet excited state (T_1) excitons are transferred from the host to the phosphorescent sensitizer via Förster resonance energy transfer (FRET) and Dexter energy transfer (DET) processes, respectively. The phosphorescent sensitizer leverages the spin-orbit coupling effect of heavy metal atoms to efficiently convert S_1 excitons into T_1 excitons via intersystem crossing (ISC). The T_1 excitons are then transferred to the S_1 state of the emitter through the FRET process.[43] The key step in this energy transfer cascade is the transfer of T_1 exciton energy from the sensitizer to the S_1 excitons of the emitter via FRET, thereby reducing the generation of long-lived T_1 excitons in the TADF emitter.[44] Additionally, selecting the phosphorescent sensitizer with a triplet state energy level (E_T) closely matching the singlet energy level (E_s) of the MR-TADF emitter enables filtering the S_1 excitons of the emitter through reverse DET, further minimizing T_1 exciton accumulation in the emitter.[38] Since the T1 exciton lifetime of the phosphorescent sensitizer is typically shorter than that of the boron-based MR-TADF emitters, this method effectively reduces T_1 exciton density and shortens exciton lifetimes while preserving the high external quantum efficiency (EQE) and pure color emission characteristic of the MR-TADF emitters.[45–48]

In this work, we present the first PHC host-based phosphorescence-sensitized MR-TADF OLEDs. To achieve high E_T and a wide energy gap (E_g), the design strategy involves disrupting the π-conjugation of the 9,9′-spirobifluorene (SBF) skeleton by introducing peripheral *meta*-terphenyl (mtp) units. Four positional isomers of SBF were investigated: **1,6-dimtp-SBF**, **1,8-dimtp-SBF**, **3,3-dimtp-SBF** and **4,4-dimtp-SBF** (Scheme 1). These substitution patterns are very rarely reported in the literature but appear herein interesting to reach the necessary electronic and physical properties for the targeted applications. All PHC host materials exhibited high E_T values, wide E_g and excellent thermal stability, with high decomposition (T_d) and glass transition (T_g) temperatures. When used as host materials in blue MR-TADF OLEDs employing 2,6-Bis(3,6-di-tert-butyl-9H-carbazol-9-yl)boron (DtBuCzB, see structure in Figure S55) as the emitter, these isomers demonstrated outstanding EL performance. Devices sensitized with FIrpic and *fac*-Ir(tpz)$_3$ (see structures in Figure S55) produced narrowband emission peak at 488 nm, full-width at half-maximum (FWHM) of 29–30 nm and high maximum EQE (EQE_{max}) ranging from 29.1 % to 33.9 %, with minimal efficiency roll-off. Among the isomers, **1,8-dimtp-SBF** and **4,4-dimtp-SBF** showed significantly enhanced current and power efficiencies (CE and PE). Additionally, blue MR-TADF OLEDs incorporating *ν*-DABNA (see structure in Figure S55) and using **1,8-dimtp-SBF** and **4,4-dimtp-SBF** as host, in combination with CN–Ir as sensitizer, achieved narrowband emissions at 468 nm and short FWHMs of 21 nm. These devices also reached a very high EQE_{max} of approximately 31 % owing to their excellent molecular orientation, which maximizes the light outcoupling efficiency (η_{out}). These findings show the versatility of PHC materials and their great potential for achieving the new generation of high-efficiency OLEDs.

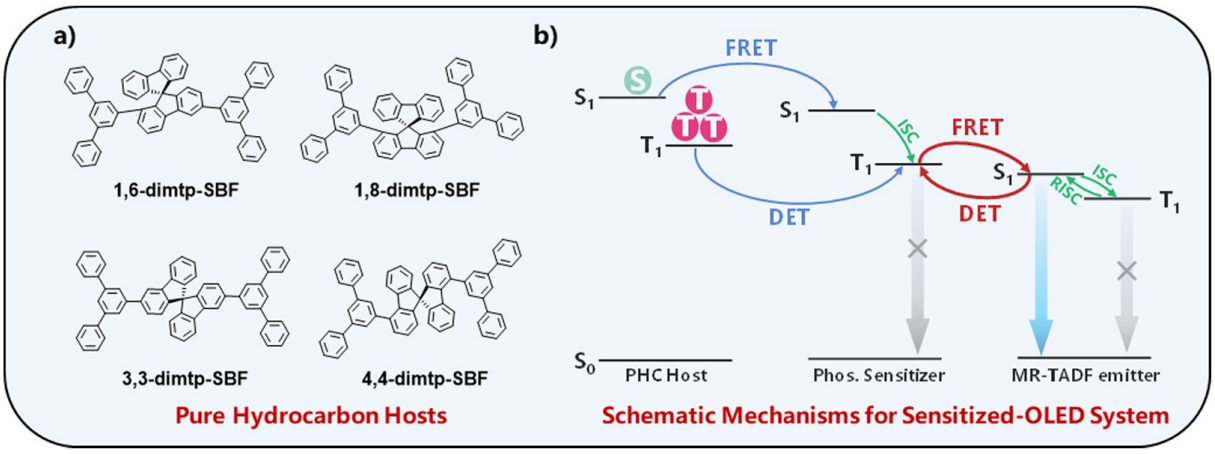

Figure 1. a) Molecular structures of four pure hydrocarbon isomers; b) The energy transfer process of the phosphorescence-sensitized system.

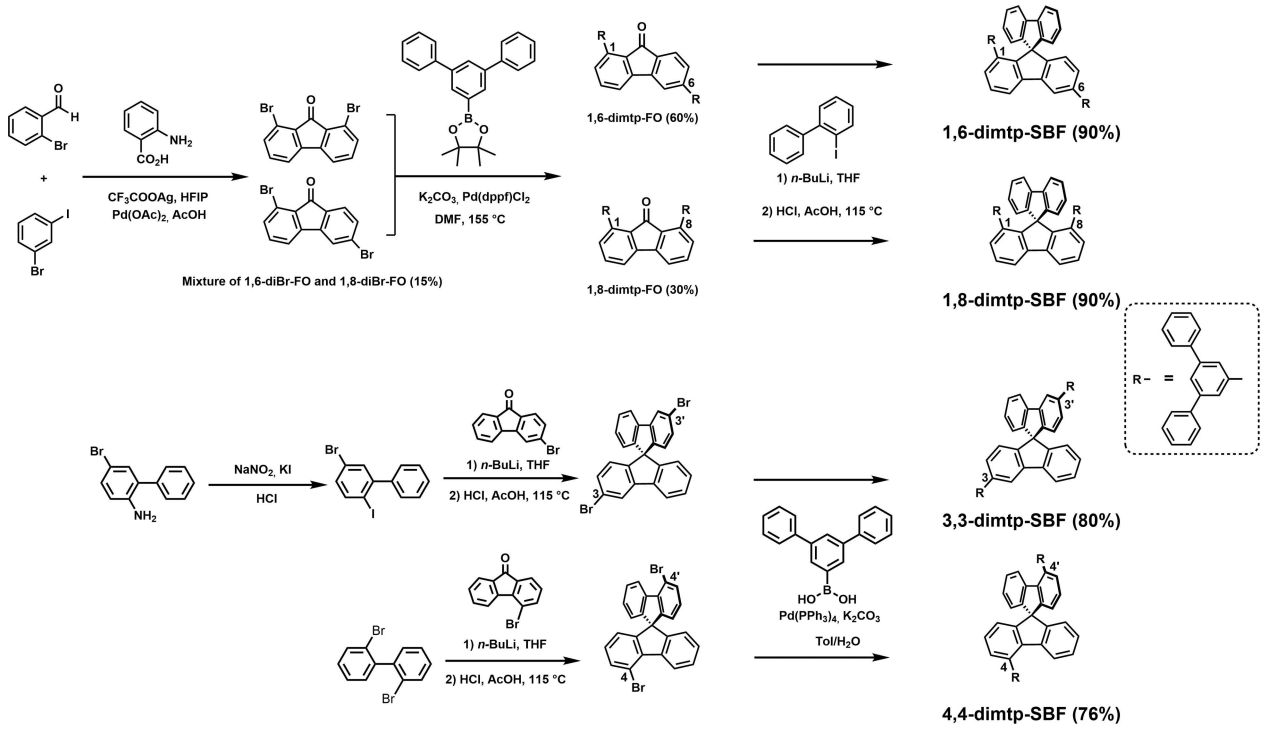

Scheme 1. Synthesis of **1,6-dimtp-SBF**, **1,8-dimtp-SBF**, **3,3-dimtp-SBF** and **4,4-dimtp-SBF**.

Results and Discussion

The synthetic route is shown in Scheme 1. The synthesis of **1,6-dimtp-SBF** and **1,8-dimtp-SBF** involves first the synthesis of the corresponding fluorenones, possessing the anchor points at C1 & C6 for **1,6-diBr-FO** and at C1 & C8 for **1,8-diBr-FO**. These substitution patterns are very rarely reported in the literature and are difficult to reach from a synthetic point of view. These compounds were synthesized using a one-pot carbon-hydrogen activation and cyclization approach, first reported by Sorensen and co-workers in 2017.[49–50] This approach is interesting as it allows to form in a single step two sophisticated fluorenyl cores with a 1,6 and 1,8-substitution pattern. As the separation of **1,6-diBr-FO** and **1,8-diBr-FO** was challenging, the grafting of the mtp fragment was performed on the mixture via a Suzuki-Myaura cross-coupling reaction yielding **1,6-dimtp-FO** and **1,8-dimtp-FO** were performed by flash chromatography. The spirofluorene unit was finally introduced with a classical sequence involving a nucleophilic addition reaction of either **1,6-dimtp-FO** or **1,8-dimtp-FO** with the lithiated biphenyl followed by an intramolecular cyclization reaction giving **1,6-dimtp-SBF** and **1,8-dimtp-SBF**. The synthesis of **3,3-dimtp-SBF** and **4,4-dimtp-SBF** was achieved via Suzuki–Miyaura coupling between the corresponding bromo-SBF and mtp-boronic acid. This synthetic route is straightforward, with yields exceeding 70 % and it supports reactions on a gram scale. Additionally, it offers a new synthetic strategy for the functionalization of the spirofluorene unit at opposite fluorene positions. The four regioisomers can only be differentiated by the SBF substitution patterns (C1, C3, or C4). These substitution sites limit the electronic coupling between the external mtp groups and the central SBF. Such design features are expected to optimize the hosting properties in OLEDs.

To better understand the configurations of the four isomers, single-crystal X-ray diffraction analyses were performed (Figure 2, Table S6–S9). The analysis revealed that all isomers possess a rigid orthogonal configuration in the SBF core, with a dihedral angle of approximately 90° between the two fluorene units (Figure S37). The dihedral angles between the SBF core and the mtp groups were also measured (Figure 2) and summarized in Table S10, with further discussion provided below. The number of intramolecular short contacts of π…π, C–H…π and C–H…H–C types is substantial across all PHC molecules studied (Figure S38–S42). These contacts contribute to structural rigidity and stabilize specific conformations, highlighting the pronounced steric hindrance within these systems, particularly at the C1 and C4 positions known for their high steric demands.[53] Distinct patterns of intermolecular interactions are also observed across the molecules (Figure S43–S47). For **1,6-dimtp-SBF**, only a single short C–H…H–C contact is present, influencing the packing arrangement and leading to a less dense crystal structure. In contrast, **1,8-dimtp-SBF** exhibits a relatively greater number of intermolecular short contacts, with C–H…π interactions contributing to the packing. **3,3-dimtp-SBF** displays three types of intermolecular interactions C–H…π, π…π and C–H…H–C resulting in a more compact crystal structure than those of **1,6-dimtp-SBF** and **1,8-dimtp-SBF**. The crystal structure of **4,4-dimtp-SBF** is particularly noteworthy, as it includes two distinct con-

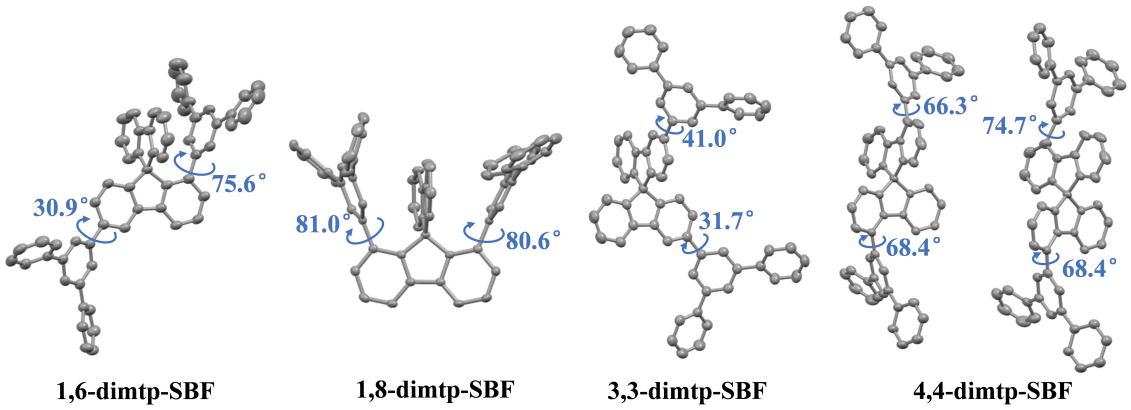

Figure 2. Single crystal configuration of **1,6-dimtp-SBF**, **1,8-dimtp-SBF**, **3,3-dimtp-SBF** and **4,4-dimtp-SBF**. Hydrogen atoms have been omitted for clarity.

formers. The first conformer exhibits a remarkably high number of intermolecular short contacts, involving three types of interactions: C–H…π, π…π and C–H…H–C, producing an extremely dense and compact crystal structure. Conversely, the second conformer shows significantly fewer interactions, with only C–H…π contacts. This reveals the coexistence of two very distinct conformers in the crystal: one with a high number of short intermolecular contacts and another with a low number of interactions, which suggests the possibility of polymorphism in the crystalline structure of **4,4-dimtp-SBF**. These intermolecular interactions drive molecular packing, which can substantially influence device performance by promoting charge transfer and improving thermal stability. Additionally, owing to the presence of the large and twisted mtp substituents, all four isomers exhibit a loose molecular packing arrangement (Figure S48), which significantly reduces strong π…π interactions between molecules, thereby minimizing intermolecular quenching. This loose packing facilitates the horizontal orientation of molecules in films, enhancing η_{out} and improving OLED performance.[51] This will be demonstrated below. These findings reveal the potential of this series of isomers as promising host materials for OLED applications.

As the PHC concept is based on the stability of the C–H and C–C bonds *vs* C–N, C–O or C–S bonds, Bond Dissociation Energies (BDE) were evaluated on different SBF-based models (Figure S54). Independently of the substitution position (C1, C3 or C4), the BDEs of C–H and C–C bonds were always higher than those of C–N, C–O or C–S bonds in corresponding model compounds.

As shown in Figure 3a, the UV/Visible absorption spectra of the four isomers in diluted cyclohexane solution (10^{-5} M) exhibit significant differences translating the importance of the substitution pattern. Time-dependent density functional theory (TD-DFT) calculations, using the B3LYP functional and def2svp basis set, were performed on the optimized ground (S_0) state geometries (Figure S49, Table S11–S14). All four isomers display a characteristic absorption band between 308 and 316 nm, corresponding to the SBF backbone.[52,53] Additionally, red-shifted absorption bands at longer wavelengths were observed, indicating electronic coupling between the fluorene fragment and the terphenyl substituents.[53] Among the isomers, the absorption spectrum of **1,8-dimtp-SBF** is the most similar to that of **SBF**. TD-DFT studies reveal that while the bathochromic-shifted absorption band remains present in **1,8-dimtp-SBF**, its intensity is relatively low, indicating that the C1 position has a smaller influence on absorption properties compared to positions C3 and C4. Indeed, the C1 position presents the advantages of both C3 and C4 positions, namely an electronic decoupling thanks to the *meta*-linkage (as for C3) and a high steric hindrance (as for C4). The high sterically hindered environment of **1,8-dimtp-SBF** is materialized by the large dihedral angles, measured in the crystallographic structure (80.6°/81.0°, Figure 2 and Table S10), between the fluorene and the mtp. In contrast, **3,3-dimtp-SBF** exhibits a particularly intense bathochromic-shifted absorption band, reflecting an extension of the π-conjugation. This π-extension at the C3 position has been discussed elsewhere.[52–53] As a result, the absorption intensity of **1,6-dimtp-SBF** lies between that of **3,3-dimtp-SBF** and **1,8-dimtp-SBF** with a shoulder at ca. 316 nm translating the electronic coupling induced by the position C3. The spectrum of **4,4-dimtp-SBF** also shows this shoulder at ca. 316 nm, which reflects a certain degree of π-conjugation between the fluorene and mtp units. However, the large angle formed between the fluorene and the mtp at the C4 position (66.3°/68.4°/74.7°, Figure 2) significantly disrupts π-conjugation in **4,4-dimtp-SBF**. This strong steric congestion is the main characteristic of the C4 position.[4,54] To further validate the steric hindrance effects in the four isomers, we performed the Independent Gradient Model based on Hirshfeld (IGMH) analysis (Figure S53). In summary, the C1 position effectively disrupts the π-conjugation because of the cumulative effect of a strong steric hindrance and *meta*-substitution, while the C3 and C4 positions cause only partial disruption of π-conjugation due to only one of these effects (*meta*-linkage for C3 and steric hindrance for C4). Based on the onset of the absorption spectra, the E_g^{opt} of **1,8-dimtp-SBF**, **4,4-dimtp-SBF**, **3,3-dimtp-SBF** and **1,6-dimtp-SBF** are estimated to be 3.85, 3.79, 3.76 and 3.72 eV, respectively (Table 1). Compared to the E_g^{opt} of **SBF** (3.97 eV), there is

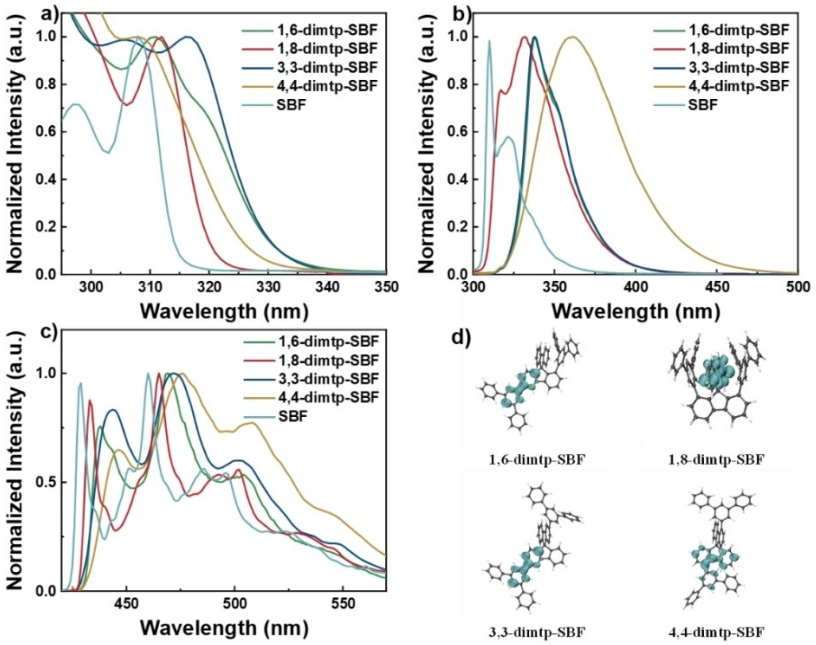

Figure 3. (a) Absorption and (b) fluorescence spectra at room temperature in cyclohexane (c) phosphorescence spectra in 2-methyl-THF at 77 K and (d) spin density distribution (SDD) of the triplet state of **1,6-dimtp-SBF**, **1,8-dimtp-SBF**, **3,3-dimtp-SBF** and **4,4-dimtp-SBF**.

Table 1: Selected properties of **1,6-dimtp-SBF**, **1,8-dimtp-SBF**, **3,3-dimtp-SBF** and **4,4-dimtp-SBF**. **SBF** is reported herein for comparison.[53,55]

	1,6-dimtp-SBF	1,8-dimtp-SBF	3,3-dimtp-SBF	4,4-dimtp-SBF	SBF
λ_{abs} [nm][a]	311, 318	312	306, 316	308	308
λ_{em} [nm][a]	338	317, 332	338	361	310, 323
Φ	0.65[b]	0.24[b]	0.60[b]	0.61[b]	0.55[c]
λ_{phos} [nm][d]	438	433	444	446	429
τ_f [ns][a]	7.47	8.30	7.58	3.63	4.6
k_r ($\times 10^7$) [s^{-1}]	8.70	2.89	7.91	16.80	12
k_{nr} ($\times 10^7$) [s^{-1}]	4.69	9.15	5.28	10.74	10
$\tau_{p\ (s)}$	5.33	5.70	4.46	4.14	5.4
E_S [eV][e]	3.86	4.04	3.87	3.82	4.05
E_T [eV][f]	2.83	2.86	2.82	2.78	2.89
LUMO $_{El}$ [eV][g]	−2.08	−1.93	−2.09	−2.12	−1.74
LUMO $_{th}$ [eV]	−1.35	−1.32	−1.35	−1.38	−1.26
HOMO $_{El}$ [eV][h]	−5.93	−5.84	−5.97	−6.01	−5.95
HOMO $_{th}$ [eV]	−5.80	−5.71	−5.88	−5.97	−5.99
E_g^{el} [eV]	3.85	3.91	3.88	3.89	4.14
E_g^{opt} [eV][i]	3.72	3.85	3.76	3.79	3.97
T_g [°C]	150	127	172	164	–
T_d [°C]	435	407	490	463	234
μ_h ($\times 10^{-6}$) [$cm^2\ V^{-1}\ s^{-1}$][j]	9.26	6.94	8.75	7.58	–
μ_e ($\times 10^{-6}$) [$cm^2\ V^{-1}\ s^{-1}$][j]	4.04	3.23	2.52	6.81	–
μ_h / μ_e	2.29	2.14	3.47	1.13	–

[a] In cyclohexane. [b] Compared to SBF. [c] Compared to quinine sulfate. [d] In 2-methyl-THF at 77 K. [e] Calculated from the onset of the highest energy band in cyclohexane (1239.84/λ). [f] Calculated from the peak maximum of the highest energy phosphorescent band, (1239.84/λ), at 77 K in 2-MeTHF. [g] From CVs in DMF. [h] From CVs in DCM. [i] Calculated from the onset of the UV/Vis absorption spectrum in cyclohexane. [j] Hole/electron mobility. th = theoretical, el = electrochemical, opt = optical.

hence a significant reduction of E_g^{opt}, reflecting the varying degrees of π-conjugation disruption as a function of the substitution pattern. These results suggest that these materials are promising candidates as host materials for OLEDs.

The emission characteristics are also significantly influenced by the substitution pattern (Figure 3b). The **1,8-dimtp-SBF** displays the bluest emission spectrum (λ_{max} = 317 and 332 nm) with only a slight bathochromic shift compared to **SBF** (λ_{max} = 310 and 323 nm), as also observed above in absorption. Surprisingly, the fluorescence spectra of **1,6-dimtp-SBF** and **3,3-dimtp-SBF** are nearly identical, both exhibiting a moderate bathochromic shift (λ_{max} = 338 nm). It

is well established that the position C3 of a fluorene (similar to the C2 position) leads to a planification of S_1,[53] which can erase the linkage effects and usually induces a bathochromic shift of the emission and a relatively narrow spectrum as observed for both **1,6-dimtp-SBF** and **3,3-dimtp-SBF**. The root-mean-square deviation (RMSD) of **4,4-dimtp-SBF** is calculated to be 1.06 Å, revealing that the deformation and fluctuation of geometric configurations between S_0 and S_1 states of **4,4-dimtp-SBF** are large during the electronic transition process (Figure S51). Additionally, the calculated reorganization energies for **1,6-dimtp-SBF**, **1,8-dimtp-SBF**, **3,3-dimtp-SBF** and **4,4-dimtp-SBF** are 0.78, 0.59, 0.56 and 1.09 eV, respectively. Among the four isomers, **4,4-dimtp-SBF** exhibits the largest reorganization energy (Table S15), resulting in the largest Stokes shift and the largest bathochromic shift in fluorescence emission, consistent with experimental observations ($\lambda_{max}=361$ nm). C4-substituted SBFs have previously been the subject of several studies to shed light on their unusual fluorescence properties and the present findings are in accordance with other C4-substituted SBFs reported in the literature.[4,53–54] The quantum yields (Φ) were measured at 0.65, 0.24, 0.60 and 0.61 for **1,6-dimtp-SBF**, **1,8-dimtp-SBF**, **3,3-dimtp-SBF** and **4,4-dimtp-SBF** respectively. Except for **1,8-dimtp-SBF**, all the quantum yields are similar to that of **SBF** (0.55). The highest value observed for **1,6-dimtp-SBF** can be related to the combination of a low non-radiative constant k_{nr} and a relatively high radiative constant k_r (4.69 and 8.70×10^7 s^{-1} respectively, Table 1). The two smallest k_{nr} in the series are detected for the two compounds possessing relaxed C3 linkages, **1,6-dimtp-SBF** and **3,3-dimtp-SBF**, without strong steric hindrance. Oppositely, in both **1,8-dimtp-SBF** and **4,4-dimtp- SBF**, the steric congestion induced by the position C1 or C4 increases k_{nr} to 9.15×10^7 and 1.07×10^8 s^{-1} respectively. In the case of **4,4-dimtp-SBF**, Φ is maintained high since k_r is also measured very high, 1.68×10^8 s^{-1}, in accordance with a high oscillator strength of the HOMO/LUMO transition (f = 0.0996). Oppositely, for **1,8-dimtp-SB**, the combination of low k_r (2.89×10^7 s^{-1}) and high k_{nr} (9.15×10^7 s^{-1}) leads to a dramatic drop of Φ. In the latter, the C1 position is at the origin of this feature with an almost null oscillator strength for the HOMO/LUMO transition ($f=0.0001$) and a highly sterically hindered environment. This is in line with previously reported results on C1-substituted SBFs.[27,53]

The phosphorescence emission spectra recorded at 77 K in 2-MeTHF (Figure 3c) provide the E_T values for **1,8-dimtp-SBF**, **1,6-dimtp-SBF**, **3,3-dimtp-SBF** and **4,4-dimtp-SBF**, which are estimated to be 2.86, 2.83, 2.82 and 2.78 eV, respectively. Contrary to our observations from absorption and fluorescence, the nature of the linkage fully drives the E_T values. **1,8-dimtp-SBF** exhibits the highest E_T, reflecting its effective disruption of π-conjugation, with an E_T value very close to that of unsubstituted **SBF** (2.89 eV). This results from the combination of two *meta* linkages and a constrained environment, with dihedral angles between the SBF core and the mtp units of 89.2°/89.3° in the T_1 state (Figure S52 and Table S16). In contrast, **1,6-dimtp-SBF** and **3,3-dimtp-SBF**, which both possess C3 substitution patterns, display lower E_T values of 2.83 eV and 2.82 eV, respectively, with T_1-state dihedral angles of 5.0°/73.8° and 7.1°/39.1°. These E_T values are nevertheless higher than that of **4,4-dimtp-SBF**, which features *ortho* linkages (C4) and has an E_T value of 2.78 eV, with T_1-state dihedral angles of 33.5°/62.4°. This feature can be illustrated by the spin density distribution (SDD, Figure 3d). Indeed, **1,8-dimtp-SBF** shows spin density fully localized on a single fluorene unit, while **4,4-dimtp-SBF** exhibits partial delocalization on the mtp unit, explaining the lower E_T value. The C3 linkage of **1,6-dimtp-SBF** and **3,3-dimtp-SBF** provides spin densities concentrated on two phenyl rings, one of the fluorene and one of the mtp, resulting in E_T that are intermediate between those of the two other isomers. Additionally, these compounds exhibit relatively long T_1 state lifetimes, estimated to range from 4.14 to 5.70 s. In summary, the E_T values of these four isomers can be finely modulated through different substitution patterns but are, for all, maintained very high, which is an essential feature for achieving efficient energy transfers in OLEDs.

The electrochemical properties of the four isomers were examined using cyclic voltammetry (CV) in CH_2Cl_2 (for oxidation) and DMF (for reduction), as presented in Figure S26–S35 and summarized in Table 1. From the onset oxidation potentials, HOMO energy levels for **1,6-dimtp-SBF**, **1,8-dimtp-SBF**, **3,3-dimtp-SBF** and **4,4-dimtp-SBF** were evaluated at −5.93, −5.84, −5.97 and −6.01 eV, respectively. The HOMO energy levels can be classified in two sets: one possessing HOMO energy levels higher than that of **SBF** (−5.95 eV), namely **1,6-dimtp-SBF** and **1,8-dimtp-SBF** (−5.93, −5.84 eV) and one surprisingly lower than that of **SBF**, namely **3,3-dimtp-SBF** and **4,4-dimtp-SBF** (−5.97 and −6.01 eV). Thus, the **3,3-dimtp-SBF/4,4-dimtp-SBF** couple appears to be more difficult to oxidize than the **SBF** building unit, indicating an electron-withdrawing effect of the mtp fragment on the SBF core. This electron-withdrawing effect of the mtp core seems to have more influence than the π-conjugation extension induced by the fluorene/mtp connection. Their HOMO energies are therefore lowered compared to that of **SBF**. The strongest effect on the HOMO energy is thus logically detected for **4,4-dimtp-SBF**, which possesses two *ortho* linkages.

Compounds **1,6-dimtp-SBF** and **1,8-dimtp-SBF** display drastically different behavior. Indeed, in the case of **1,8-dimtp-SBF**, the presence of the two mtp at C1 induces strong cofacial interactions.[56–57] Such interactions are known to significantly decrease the HOMO energy levels.[58–62] This can be seen by the electronic density born by the two mtp in the HOMO (Figure 4), which is characteristic of such types of interactions. For **1,6-dimtp-SBF**, which possesses only one mtp fragment at C1, this effect is logically diminished and the HOMO is then lowered. Thus, three different effects are involved in this series: (i) Through-space interaction because of the substitution at C1, (ii) through-bond extension of the π-conjugation and (iii) electron-withdrawing effect of the mtp fragment.

The reduction potentials were measured in DMF providing peak potentials of −2.48, −2.32, −2.31 and −2.28 V for **1,8-dimtp-SBF**, **1,6-dimtp-SBF**, **3,3-dimtp-SBF** and **4,4-**

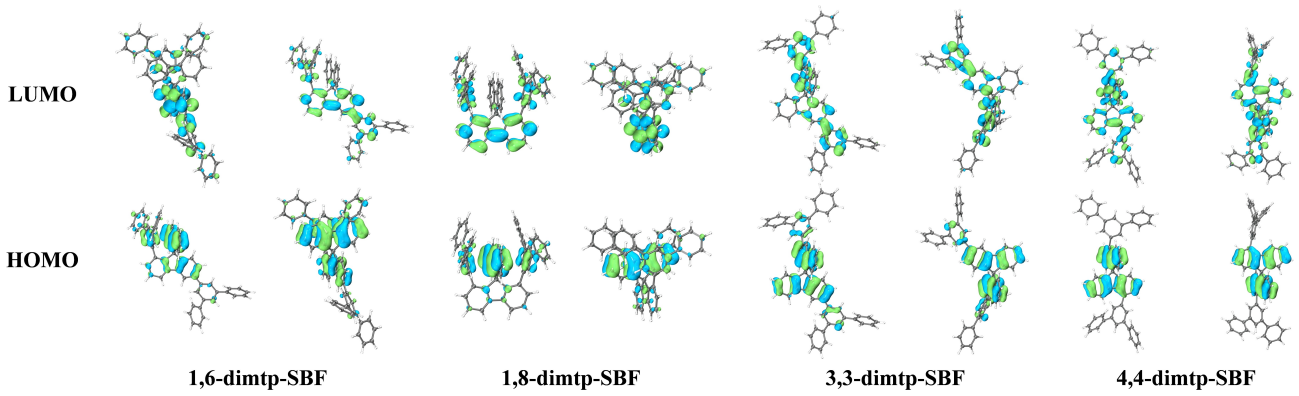

Figure 4. Frontier molecular orbitals of **1,6-dimtp-SBF**, **1,8-dimtp-SBF**, **3,3-dimtp-SBF** and **4,4-dimtp-SBF**. (top: LUMO, bottom: HOMO, B3LYP, def2svp, isovalue of 0.035[ebohr^{-3}]$^{1/2}$).

dimtp-SBF respectively. Corresponding LUMO energy levels were evaluated at −1.93, −2.08, −2.09 and −2.12 eV. Oppositely to what was observed for the HOMO energies, the electron-withdrawing effect of the mtp groups is predominant in the LUMOs, depressing for all molecules the LUMO energy levels compared to **SBF** (−1.74 eV). Specifically, the LUMO of **1,6-dimtp-SBF** and **1,8-dimtp-SBF** is mainly localized on the substituted fluorene (because of the substitution on a single fluorene), while the LUMO of **3,3-dimtp-SBF** and **4,4-dimtp-SBF** is distributed across both the SBF backbone and the attached benzene rings (owing to the substitution on two fluorenes). For the latter, this leads to a deepening of the LUMO energy. The deep HOMO and high LUMO energy levels provide wide E_g of 3.91, 3.89, 3.88 and 3.85 eV for **1,8-dimtp-SBF**, **4,4-dimtp-SBF, 3,3-dimtp-SBF** and **1,6-dimtp-SBF** respectively. This wide E_g effectively prevents holes and electrons from recombining directly within the host material, which facilitates efficient energy transfer of the sensitization system and enhances emission efficiency. This is crucial for incorporating emitter and phosphorescent sensitizers into the OLED emission layer (EML).

The PHC constructed on the SBF skeleton offers significant morphological stability and high thermal stability, which can reduce efficiency roll-off owing to heat accumulation and material degradation. Thermogravimetric analysis (TGA) and differential scanning calorimetry (DSC) were employed to assess the thermal and morphological properties of the four isomers. The results show that these compounds exhibit excellent thermal stability (Figure S36). The T_d measured at 5 % mass loss, are 435, 407, 490 and 463 °C for these isomers, indicating their robust thermal stability. Additionally, the T_g are significantly high, recorded at 150, 127, 172 and 164 °C (Table 1). The variations are primarily attributed to the different molecular arrangements of the isomers, highlighting the impact of the substitution patterns on this characteristic. In contrast, the thermal stability of the **SBF** building block is comparatively low, with a T_d of 234 °C.[53,55] These findings show that these host materials display high thermal stabilities while maintaining the favorable electronic properties of **SBF**, including high E_T and wide E_g.

Before examining the EL characteristics, we first analyzed hole-only and electron-only devices (HOD and EOD) to measure charge mobility (Figure S56). At low bias, the curves were well-fitted within the space-charge-limited current (SCLC) region. The calculated zero-field mobilities of the compounds are summarized in Table 1. Consistent with other PHC systems reported in the literature, all compounds demonstrated good charge balance owing to their comparable hole and electron mobilities. This charge balance is crucial for enhancing OLED performance, as it facilitates efficient recombination of holes and electrons, contributing to the high efficiency observed in subsequent studies, particularly for the new generations of simplified OLEDs called Single-Layer.[21,63–64] This behavior is partially attributed to the inherent PHC properties of these host materials as previously observed in the literature.[31–33] Indeed, for hosts containing heteroatoms, achieving balanced charge transport can be challenging due to the intrinsic properties of their functional units, which may be either electron-rich or electron-deficient.

Finally, as the four isomers displayed all the prerequisites, they were employed as hosts in MR-TADF OLEDs. To reduce the likelihood of exciton formation through direct charge trapping on the emitter, phosphorescent sensitizers (FIrpic, *fac*-Ir(tpz)$_3$, CN–Ir)[38,65–66] were selected with HOMO energy levels closely matching that of the emitters (DtBuCzB and *ν*-DABNA)[67–68] (Table S22). Additionally, to maximize the spectral overlap between the photoluminescence (PL) of the sensitizer and the absorption spectrum of the emitter, thereby enhancing FRET efficiency of energy transfer from T_1 excitons of the sensitizer to S_1 excitons of the emitter, we measured the overlap between the PL spectra of the sensitizers and the absorption spectra of the emitters in diluted toluene solution (Figure S57). The results indicate the large spectral overlap, which effectively optimizes device performance by minimizing energy loss and improving emission efficiency. Furthermore, to suppress T_1 exciton exchange from the T_1 state of the sensitizer to the T_1 state of the emitter via DET, the emitter doping concen-

tration was maintained between 0.5 and 2 wt %, ensuring sufficient spatial separation between the sensitizer and the emitter.[69–72] The OLEDs investigated present the following structure: ITO/HAT-CN (10 nm)/TAPC (40 nm)/TCTA (10 nm)/mCP (10 nm)/ EML (20 nm)/TmPyPB (40 nm)/Liq (2 nm)/Al (80 nm). In this configuration, HAT-CN (1,4,5,8,9,11-hexaazatriphenylenehexacarbonitrile) acts as the hole injection layer, TAPC (1,1-bis[(di-4-tolylamino)phenyl]cyclohexane) and TCTA (Tris(4-carbazoyl-9-ylphenyl)amine) serve as hole transport layers, mCP (1,3-bis-(*N*-carbazolyl)benzene)) functions as an electron-blocking layer and TmPyPB (1,3,5-tri(m-pyridin-3-ylphenyl)benzene) and Liq (lithium-8-hydroxyquinolinolate) are used as the electron transport and electron injection layers, respectively. The EML consists of the host material mixed with 2 wt % of DtBuCzB and 10 wt % of FIrpic. The EL performance of the OLEDs is depicted in Figure 5 and Figure S58, while the device structure, energy level diagram and molecular structures of the functional materials are presented in Figure S55. The device performances are summarized in Table 2.

As shown in Figure 5 and Figure S58, devices D1–D4 exhibit similar EL spectra, with a maximum of 488 nm and a FWHM of 30 nm. Their driving voltages are respectively 3.71, 3.72, 3.79 and 3.79 V at 0.01 mA cm^{-2}, indicating excellent charge injection properties. Remarkably, all devices achieve exceptionally high EQE$_{max}$, ranging from 29.1 % to 33.9 %. Devices D2 and D4, based on **1,8-dimtp-SBF** and

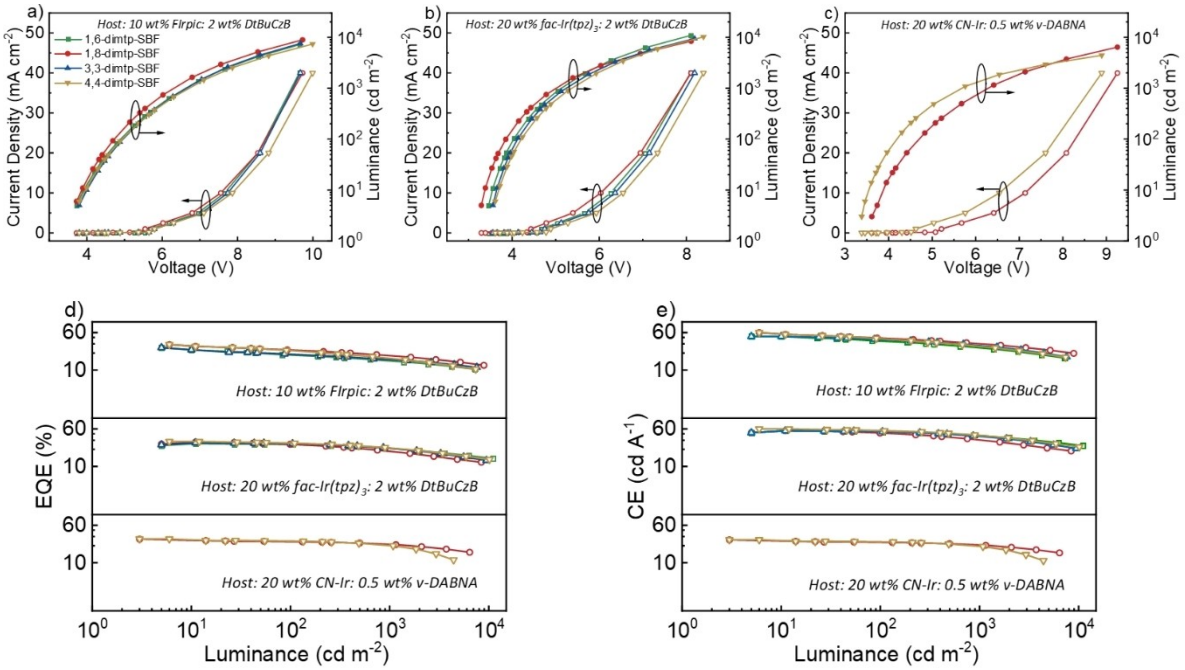

Figure 5. Device performance of D1-B2 using **1,6-dimtp-SBF**, **1,8-dimtp-SBF**, **3,3-dimtp-SBF** and **4,4-dimtp-SBF** as host. Current density and luminance versus driving voltage (*J–V–L*) characteristics for a) D1-D4; b) D5-D8; c) B1 and B2. d) EQE versus luminance characteristics for D1-D4 (top), D5-D8 (middle) and B1-B2 (bottom). e) CE versus luminance characteristics for D1-D4 (top), D5-D8 (middle) and B1-B2 (bottom).

Table 2: Summary of OLED device performance.

EML	Host	V^a (V)	$\lambda_{EL}{}^b$ (nm)	FWHM^b (nm)	CE^c (cd A^{-1})	PE^c (lm W^{-1})	EQE^d (%)	$\Theta_h{}^e$
Host: 10 wt% FIrpic: 2 wt% DtBuCzB	1,6-dimtp-SBF (D1)	3.71	488	30	50.0	42.2	29.1/15.5	82
	1,8-dimtp-SBF (D2)	3.72	488	30	60.0	54.1	33.9/20.0	84
	3,3-dimtp-SBF (D3)	3.79	488	30	50.0	41.4	29.3/16.7	84
	4,4-dimtp-SBF (D4)	3.79	488	30	60.0	49.7	33.9/17.6	89
Host: 20 wt% *fac*-Ir(tpz)$_3$: 2 wt% DtBuCzB	1,6-dimtp-SBF (D5)	3.46	488	30	55.0	48.6	29.9/23.8	81
	1,8-dimtp-SBF (D6)	3.29	488	29	55.0	51.1	32.0/20.6	82
	3,3-dimtp-SBF (D7)	3.55	488	29	55.0	47.3	31.0/23.8	84
	4,4-dimtp-SBF (D8)	3.61	488	30	60.0	52.2	32.9/24.2	89
Host: 20 wt% CN-Ir: 0.5 wt% ν-DABNA	1,8-dimtp-SBF (B1)	3.61	468	21	30.0	26.1	30.9/23.6	85

[a] Driving voltages at the current density of 0.01 mA cm^{-2}. [b] Measured at a driving current density of 40 mA cm^{-2}. [c] Values of CE$_{max}$ and PE$_{max}$. [d] EQE at the maximum and 1,000 cd m^{-2}. [e] The horizontal dipole ratio.

4,4-dimtp-SBF respectively, exhibit both an extremely high EQE_{max} of 33.9 % and a maximum CE (CE_{max}) of 60 cd A^{-1}. However, D2 demonstrates a slightly higher maximum PE (PE_{max}) of 54.1 lm W^{-1} compared to 49.7 lm W^{-1} for D4, likely owing to the lower driving voltage of D2. These results represent state-of-the-art performance for OLED devices utilizing DtBuCzB. It is noteworthy that the exceptional charge balance demonstrated by **4,4-dimtp-SBF** significantly contributes to its high efficiency. Additionally, devices D1 (**1,6-dimtp-SBF**) and D3 (**3,3-dimtp-SBF**) also achieve very high EQE_{max} values respectively measured at 29.1 % and at 29.3 %. This shows the high efficiency of the whole series of materials. In OLED devices, EQE is directly influenced by the η_{out}, which depends not only on the thickness and refractive index of the materials but also on the orientation of the transition dipole moment of the emitter in the amorphous host. Specifically, horizontal molecular orientation relative to the substrate enhances both η_{out} and EQE. The orientation of MR molecules in the EML can affect efficiency. While altering the structure of MR molecules can adjust the orientation, modifying the host material, which is the main component of the EML, provides a more direct approach to achieve efficient OLEDs.[73] In order to elucidate the very high performance of the PHC series, the horizontal molecular orientation within the EML has been investigated. Thus, co-doped films ($film_1$-$film_4$) based on the EMLs of devices D1-D4 were prepared. The measurement results are presented in Figure S59.

The results indicate that the horizontal dipole ratio(Θ_h) of FIrpic and DtBuCzB in **1,6-dimtp-SBF**, **1,8-dimtp-SBF**, **3,3-dimtp-SBF** and **4,4-dimtp-SBF** are 82 %, 84 %, 84 % and 89 %, respectively. These high Θ_h are attributed to the rigidity of the host structure and the suppression of reorientation and randomization of the guest and sensitizer molecules during deposition, owing to the high evaporation temperature. These findings further enhance the EL performance of OLED devices based on PHC hosts and explain the very high EQE values reached.

To further validate the present design strategy, we used the phosphorescent material *fac*-$Ir(tpz)_3$[65] as a sensitizer for DtBuCzB to fabricate devices (D5-D8). The structure of these devices is identical to that of the previously mentioned D1-D4 devices, except that the EML doping was changed from 10 wt % FIrpic to 20 wt % *fac*-$Ir(tpz)_3$. The device structures and energy level diagrams are shown in Figure S55 and the EL performance is illustrated in Figure 5 and summarized in Table 2. Similar to the devices using FIrpic as a sensitizer, devices D5-D8 exhibited extremely high performance. These devices achieved narrow spectral emission with a maximum at 488 nm and their EQE_{max} ranged from 29.9 % to 32.9 %. Devices D6 and D8 demonstrated outstanding performance, with D6 achieving an EQE_{max} of 32.0 %, a CE_{max} of 55 cd A^{-1} and a PE_{max} of 51.1 lm W^{-1}. Device D8 exhibited an EQE_{max} of 32.9 %, a CE_{max} of 60 cd A^{-1} and a PE_{max} of 52.2 lm W^{-1}. Devices D5 and D7 also exhibited excellent performance, with the corresponding device characteristics summarized in Table 2. Notably, at high luminance levels of 1000 cd m^{-2}, D5-D8 exhibited outstanding low efficiency roll-off of 20.6 %, 35.6 %, 23.3 % and 27.0 % respectively. This is attributed to the excellent carrier balance capability of the PHC host and the short T_1 lifetime of the phosphorescent sensitizer. *fac*-$Ir(tpz)_3$ could efficiently facilitate the conversion of T_1 excitons into S_1 of DtBuCzB, thereby reducing the accumulation of T_1 excitons within the device. This reduction suppresses triplet-triplet annihilation (TTA) and triplet-polaron annihilation (TPA), effectively mitigating efficiency roll-off.[71,74] Consistent with previous findings, we also prepared co-doped films ($film_5$-$film_8$) based on the EML of devices D5-D8 to investigate the Θ_h within the EML (Figure S60). The measured Θ_h were 81 %, 82 %, 84 % and 89 %, respectively. These results show only a little variation from the data presented above, suggesting that the structure and physical properties of the host material (and not the dopant or the sensitizer) largely determine molecular arrangement within the EML. As the molecular orientation in the EML often plays a dominant role in the OLED performance, this clearly emphasizes herein the high efficiency of the overall PHC concept rather than that of individual molecules.

As blue OLEDs remain one of the most challenging areas in the field, we further explored the potential of PHC hosts with another EML association, namely CN–Ir as the phosphorescent sensitizer and *v*-DABNA as the blue MR-TADF emitter. CN–Ir exhibits an E_T (2.70 eV) comparable to the singlet energy of *v*-DABNA (2.65 eV) and possesses a relatively short triplet lifetime (1.8 μs).[38] Furthermore, there is a significant overlap between the emission of CN–Ir and the absorption of *v*-DABNA, which renders it an ideal sensitizer (Figure S57). Owing to its high E_T and wide E_g, **1,8-dimtp-SBF** exhibits superior excitonic properties, while **4,4-dimtp-SBF** ensures optimal charge balance and horizontal orientation. Consequently, these materials outperform the other two hosts in device performance, making them the primary choices for blue MR-TADF OLEDs in this study. The optimized device structures (B1 and B2) are as follows: ITO/HAT (10 nm)/TAPC (40 nm)/TCTA (10 nm)/mCP (10 nm)/0.5 wt % *v*-DABNA: 20 wt % CN–Ir: Host (20 nm)/TmPyPb (40 nm)/Liq (2 nm)/Al (80 nm). The EL spectra and device performance are shown in Figure 5, with the data summarized in Table 2. Incorporating CN–Ir into the device reduces the energy gaps between the host and emitter, as its HOMO and LUMO levels are positioned between them, facilitating carrier injection and transport within the EML (Table S22). As a result, both B1 (with **1,8-dimtp-SBF** as the host) and B2 (with **4,4-dimtp-SBF** as the host) devices exhibited low driving voltages. Additionally, these devices showed narrow blue EL spectra (FWHMs of only 21 nm), centered at 468 nm. The additional energy transfer between CN–Ir and *v*-DABNA can reduce exciton loss and achieve a very high EQE_{max} of approximately 31 %. Devices B1 and B2 also demonstrated high current CE_{max} and PE_{max}. Furthermore, similar to the devices above, devices B1 and B2 also exhibit excellent efficiency roll-off values of 21.8 % and 26.7 %, respectively. Co-doped films ($film_9$ and $film_{10}$) were prepared to measure Θ_h, which were found to be as high as 85 % and 93 % (Figure S61). This orientation is one important reason involved in the excellent efficiency and low roll-off observed in these devices.[75] At high current

densities, enhanced electric fields usually cause polarization effects, altering molecular orientation within the EML and leading to efficiency degradation.[76] However, using PHC materials as hosts can stabilize molecular orientation, mitigating polarization effects and maintaining high EQE levels even at high luminance.

To further validate the high performance of this series of devices, transient PL measurements were conducted to examine the photophysical properties of the EML (Figure S62). Films ($film_{11}$ and $film_{12}$) were prepared by co-doping CN–Ir and *ν*-DABNA with **1,8-dimtp-SBF** and **4,4-dimtp-SBF** as host materials, respectively. The PL quantum yields (PLQY) of $film_{11}$ and $film_{12}$ were measured at 95 % and 96 %, respectively. Importantly, the PLQY of the co-doped films remained high despite energy transfer processes, which is critical for achieving high device efficiency. Using the PLQY values and decay times, the reverse intersystem crossing (k_{RISC}) rates were calculated to be $2.71\times10^6\ s^{-1}$ and $3.67\times10^6\ s^{-1}$ (film parameters summarized in Table S23). This evidence reinforces the soundness of our molecular design and the viability of PHC materials as host materials for phosphorescent-sensitized devices.

Conclusion

In the present work, we report a series of four PHC host materials constructed on the original and uncommon di-substitution of the SBF backbone. By strategically disrupting the π-conjugation of the SBF backbone, high E_T and wide E_g were achieved, which are essential characteristics for efficient energy transfers in the EML. The introduction of mtp substituents was particularly efficient in fine-tuning the electronic and optical properties of these regioisomers, confirming the role played by positional isomerism in electronics.[77] The whole series of devices displays very high performances with different phosphorescent sensitizers (FIrpic, *fac*-Ir(tpz)$_3$, CN–Ir) and emitters (DtBuCzB and *ν*-DABNA). Particularly, *ν*-DABNA-based blue OLEDs (468 nm) have reached impressive performance with EQE_{max} above 30 % and narrow FWHMs of 21 nm. We have demonstrated that PHC hosts stabilize molecular orientation and significantly reduce efficiency roll-off, which are two key features in OLEDs. This study marks the first application of PHC materials as hosts in phosphorescence-sensitized MR-TADF OLEDs, highlighting their great potential as promising candidates for next-generation blue OLEDs and offering a viable pathway to achieve high-performance devices.

Acknowledgements

The authors acknowledge financial findings from the National Natural Science Foundation of China (Nos. 22175124, 62175171 and 61961160731), the Natural Science Foundation of Jiangsu Province of China (BK20220057). This work is also supported by Suzhou Key Laboratory of Functional Nano & Soft Materials, Collaborative Innovation Center of Suzhou Nano Science & Technology, the 111 Project. This work has also been financially supported by the ANR (N22-CE07-0024-*Evolution* Project). DA thanks the EUR LUMOMAT project and the Investments for the Future program ANR-18-EURE-0012 (PIPPIN) for a Ph.D. grant. KL thanks the Region Bretagne (SIMPLIFY Project) and the ANR (N22-CE07-0024-*Evolution* Project). We also thank the CRMPO (Rennes) for mass analyses and GENCI (Project N° AD010814136) for computing time.

Conflict of Interest

The authors declare no conflict of interest.

Data Availability Statement

The data that support the findings of this study are available from the corresponding author upon reasonable request.

Keywords: pure hydrocarbon host · organic light-emitting diode · phosphorescence-sensitized · multi-resonance thermally activated delayed fluorescence · Spirobifluorene · Regioisomerism

[1] G. Hong, X. Gan, C. Leonhardt, Z. Zhang, J. Seibert, J. M. Busch, S. Bräse, *Adv. Mater.* **2021**, *33*, 2005630.
[2] C. Poriel, J. Rault-Berthelot, *Adv. Funct. Mater.* **2020**, *30*, 1910040.
[3] X. Wu, D.-G. Chen, D. Liu, S.-H. Liu, S.-W. Shen, C.-I. Wu, G. Xie, J. Zhou, Z.-X. Huang, C.-Y. Huang, S.-J. Su, W. Zhu, P.-T. Chou, *J. Am. Chem. Soc.* **2020**, *142*, 7469–7479.
[4] C. Poriel, J. Rault-Berthelot, *J. Mater. Chem. C* **2017**, *5*, 3869–3897.
[5] Y.-L. Zhang, S.-Y. Yang, Z.-Q. Feng, Y.-K. Qu, D.-Y. Zhou, C. Zhong, L.-S. Liao, Z.-Q. Jiang, *Sci. Chi. Chem.* **2022**, *65*, 2219–2230.
[6] M. A. Baldo, D. F. O'Brien, Y. You, A. Shoustikov, S. Sibley, M. E. Thompson, S. R. Forrest, *Nature* **1998**, *395*, 151–154.
[7] X. Wu, C.-Y. Huang, D.-G. Chen, D. Liu, C. Wu, K.-J. Chou, B. Zhang, Y. Wang, Y. Liu, E. Y. Li, W. Zhu, P.-T. Chou, *Nat. Commun.* **2020**, *11*, 2145.
[8] X. Tang, L.-S. Cui, H.-C. Li, A. J. Gillett, F. Auras, Y.-K. Qu, C. Zhong, S. T. E. Jones, Z.-Q. Jiang, R. H. Friend, L.-S. Liao, *Nat. Mater.* **2020**, *19*, 1332–1338.
[9] S.-Y. Yang, Y.-K. Qu, L.-S. Liao, Z.-Q. Jiang, S.-T. Lee, *Adv. Mater.* **2022**, *34*, 2104125.
[10] Y.-K. Qu, Q. Zheng, J. Fan, L.-S. Liao, Z.-Q. Jiang, *Acc. Mater. Res.* **2021**, *2*, 1261–1271.
[11] X. Wu, C.-H. Wang, S. Ni, C.-C. Wu, Y.-D. Lin, H.-T. Qu, Z.-H. Wu, D. Liu, M.-Z. Yang, S.-J. Su, W. Zhu, K. Chen, Z.-C. Jiang, S.-D. Yang, W.-Y. Hung, P.-T. Chou, *J. Am. Chem. Soc.* **2024**, *146*, 24526–24536.
[12] J.-H. Lee, C.-H. Chen, P.-H. Lee, H.-Y. Lin, M.-k. Leung, T.-L. Chiu, C.-F. Lin, *J. Mater. Chem. C* **2019**, *7*, 5874–5888.
[13] Y. Wang, J. H. Yun, L. Wang, J. Y. Lee, *Adv. Funct. Mater.* **2021**, *31*, 2008332.
[14] S. Schmidbauer, A. Hohenleutner, B. König, *Adv. Mater.* **2013**, *25*, 2114–2129.

[15] H. Li, M. Hong, A. Scarpaci, X. He, C. Risko, J. S. Sears, S. Barlow, P. Winget, S. R. Marder, D. Kim, J.-L. Brédas, *Chem. Mater.* **2019**, *31*, 1507–1519.
[16] N. Lin, J. Qiao, L. Duan, L. Wang, Y. Qiu, *J. Phys. Chem. C* **2014**, *118*, 7569–7578.
[17] D. Y. Kondakov, W. C. Lenhart, W. F. Nichols, *J. Appl. Phys.* **2007**, *101*, 024512.
[18] N. Lin, J. Qiao, L. Duan, H. Li, L. Wang, Y. Qiu, *J. Phys. Chem. C* **2012**, *116*, 19451–19457.
[19] C. Poriel, J. Rault-Berthelot, *Acc. Mater. Res.* **2022**, *3*, 379–390.
[20] Y. Morinaka, H. Ito, K. J. Fujimoto, T. Yanai, Y. Ono, T. Tanaka, K. Itami, *Angew. Chem. Int. Ed.* **2024**, *63*, e202409619.
[21] C. Poriel, J. Rault-Berthelot, *Adv. Funct. Mater.* **2021**, *31*, 2010547.
[22] K.-T. Wong, Y.-L. Liao, Y.-T. Lin, H.-C. Su, C.-c. Wu, *Org. Lett.* **2005**, *7*, 5131–5134.
[23] L.-C. Chi, W.-Y. Hung, H.-C. Chiu, K.-T. Wong, *Chem. Commun.* **2009**, 3892–3894.
[24] M. Zhuo, W. Sun, G. Liu, J. Wang, L. Guo, C. Liu, B. Mi, J. Song, Z. Gao, *J. Mater. Chem. C* **2015**, *3*, 9137–9144.
[25] S. Ye, Y. Liu, C.-a. Di, H. Xi, W. Wu, Y. Wen, K. Lu, C. Du, Y. Liu, G. Yu, *Chem. Mater.* **2009**, *21*, 1333–1342.
[26] C. Poriel, R. Métivier, J. Rault-Berthelot, D. Thirion, F. Barrière, O. Jeannin, *Chem. Commun.* **2011**, *47*, 11703–11705.
[27] L. J. Sicard, H.-C. Li, Q. Wang, X.-Y. Liu, O. Jeannin, J. Rault-Berthelot, L.-S. Liao, Z.-Q. Jiang, C. Poriel, *Angew. Chem. Int. Ed.* **2019**, *58*, 3848–3853.
[28] C. Poriel, J. Rault-Berthelot, Z.-Q. Jiang, *Mater. Chem. Front.* **2022**, *6*, 1246–1252.
[29] Y. Luo, Z. Liu, G. Yang, T. Wang, Z. Bin, J. Lan, D. Wu, J. You, *Angew. Chem. Int. Ed.* **2021**, *60*, 18852–18859.
[30] Q. Li, Z. Yu, Q. Liu, Y. Guo, Z. Fu, Y. Yang, Z. Bin, D. Wu, J. Lan, *Chem. Sci.* **2024**, *15*, 10547–10555.
[31] D. Ari, Y.-J. Yang, C. Quinton, Z.-Q. Jiang, D.-Y. Zhou, C. Poriel, *Angew. Chem. Int. Ed.* **2024**, *63*, e202403066.
[32] F.-C. Kong, Y.-L. Zhang, C. Quinton, N. McIntosh, S.-Y. Yang, J. Rault-Berthelot, F. Lucas, C. Brouillac, O. Jeannin, J. Cornil, Z.-Q. Jiang, L.-S. Liao, C. Poriel, *Angew. Chem. Int. Ed.* **2022**, *61*, e202207204.
[33] Q. Wang, F. Lucas, C. Quinton, Y.-K. Qu, J. Rault-Berthelot, O. Jeannin, S.-Y. Yang, F.-C. Kong, S. Kumar, L.-S. Liao, C. Poriel, Z.-Q. Jiang, *Chem. Sci.* **2020**, *11*, 4887–4894.
[34] X. Wu, C.-H. Wang, S. Ni, C.-C. Wu, Y.-D. Lin, H.-T. Qu, Z.-H. Wu, D. Liu, M.-Z. Yang, S.-J. Su, W. Zhu, K. Chen, Z.-C. Jiang, S.-D. Yang, W.-Y. Hung, P.-T. Chou, *J. Am. Chem. Soc.* **2024**, *146*, 24526–24536.
[35] Y. Yuan, X. Tang, X.-Y. Du, Y. Hu, Y.-J. Yu, Z.-Q. Jiang, L.-S. Liao, S.-T. Lee, *Adv. Opt. Mater.* **2019**, *7*, 1801536.
[36] X. Wu, B.-K. Su, D.-G. Chen, D. Liu, C.-C. Wu, Z.-X. Huang, T.-C. Lin, C.-H. Wu, M. Zhu, E. Y. Li, W.-Y. Hung, W. Zhu, P.-T. Chou, *Nat. Photonics* **2021**, *15*, 780–786.
[37] S. Nam, J. W. Kim, H. J. Bae, Y. M. Maruyama, D. Jeong, J. Kim, J. S. Kim, W.-J. Son, H. Jeong, J. Lee, S.-G. Ihn, H. Choi, *Adv. Sci.* **2021**, *8*, 2100586.
[38] W. J. Chung, K. H. Lee, M. Jung, K. M. Lee, H. C. Park, M.-S. Eum, J. Y. Lee, *Adv. Opt. Mater.* **2021**, *9*, 2100203.
[39] X. Yang, X. Zhou, Y.-X. Zhang, D. Li, C. Li, C. You, T.-C. Chou, S.-J. Su, P.-T. Chou, Y. Chi, *Adv. Sci.* **2022**, *9*, 2201150.
[40] C. You, X.-Q. Wang, X. Zhou, Y. Yuan, L.-S. Liao, Y.-C. Liao, P.-T. Chou, Y. Chi, *ACS Appl. Mater. Interfaces* **2021**, *13*, 59023–59034.
[41] K. H. Lee, J. Y. Lee, *J. Mater. Chem. C* **2019**, *7*, 8562–8568.
[42] H. Nakanotani, T. Higuchi, T. Furukawa, K. Masui, K. Morimoto, M. Numata, H. Tanaka, Y. Sagara, T. Yasuda, C. Adachi, *Nat. Commun.* **2014**, *5*, 4016.
[43] M. A. Baldo, M. E. Thompson, S. R. Forrest, *Nature* **2000**, *403*, 750–753.
[44] E. Kim, J. Park, M. Jun, H. Shin, J. Baek, T. Kim, S. Kim, J. Lee, H. Ahn, J. Sun, S.-B. Ko, S.-H. Hwang, J. Y. Lee, C. Chu, S. Kim, *Sci. Adv.*, *8*, eabq1641.
[45] J. Lee, C. Jeong, T. Batagoda, C. Coburn, M. E. Thompson, S. R. Forrest, *Nat. Commun.* **2017**, *8*, 15566.
[46] K. Klimes, Z.-Q. Zhu, J. Li, *Adv. Funct. Mater.* **2019**, *29*, 1903068.
[47] B. Sim, J. S. Kim, H. Bae, S. Nam, E. Kwon, J. W. Kim, H.-Y. Cho, S. Kim, J.-J. Kim, *Phys. Rev. Appl.* **2020**, *14*, 024002.
[48] S. K. Jeon, J. Y. Lee, *Org. Electron.* **2015**, *27*, 202–206.
[49] X.-Y. Chen, S. Ozturk, E. J. Sorensen, *Org. Lett.* **2017**, *19*, 1140–1143.
[50] C. Poriel, L. Sicard, J. Rault-Berthelot, *Chem. Commun.* **2019**, *55*, 14238–14254.
[51] Q. Li, Z. Li, *Acc. Chem. Res.* **2020**, *53*, 962–973.
[52] L. Sicard, C. Quinton, J.-D. Peltier, D. Tondelier, B. Geffroy, U. Biapo, R. Métivier, O. Jeannin, J. Rault-Berthelot, C. Poriel, *Chem. Eur. J.* **2017**, *23*, 7719–7727.
[53] C. Poriel, C. Quinton, F. Lucas, J. Rault-Berthelot, Z.-Q. Jiang, O. Jeannin, *Adv. Funct. Mater.* **2021**, *31*, 2104980.
[54] C. Quinton, S. Thiery, O. Jeannin, D. Tondelier, B. Geffroy, E. Jacques, J. Rault-Berthelot, C. Poriel, *ACS Appl. Mater. Interfaces* **2017**, *9*, 6194–6206.
[55] S. Thiery, D. Tondelier, C. Declairieux, G. Seo, B. Geffroy, O. Jeannin, J. Rault-Berthelot, R. Métivier, C. Poriel *J. Mater. Chem. C* **2014**, *2*, 4156–4166.
[56] L. Sicard, C. Brouillac, N. Leclerc, S. Fall, N. Zimmerman, O. Jeannin, J. Rault-Berthelot, C. Quinton, C. Poriel, *Mater. Chem. Front.* **2024**, *8*, 1349–1361.
[57] L. Sicard, C. Quinton, F. Lucas, O. Jeannin, J. Rault-Berthelot, C. Poriel, *J. Phys. Chem. C* **2019**, *123*, 19094–19104.
[58] C. Brouillac, F. Lucas, D. Ari, D. Tondelier, J. Meot, M. Malvaux, C. Jadaud, C. Lebreton, J. Rault-Berthelot, C. Quinton, E. Jacques, C. Poriel, *Adv. Electron. Mater.* **2024**, *10*, 2300582.
[59] V. J. Chebny, R. Shukla, S. V. Lindeman, R. Rathore, *Org. Lett.* **2009**, *11*, 1939–1942.
[60] R. Rathore, S. H. Abdelwahed, I. A. Guzei, *J. Am. Chem. Soc.* **2003**, *125*, 8712–8713.
[61] D. Thirion, C. Poriel, F. Barrière, R. Métivier, O. Jeannin, J. Rault-Berthelot, *Org. Lett.* **2009**, *11*, 4794–4797.
[62] D. Thirion, C. Poriel, R. Métivier, J. Rault-Berthelot, F. Barrière, O. Jeannin, *Chem. Eur. J.* **2011**, *17*, 10272–10287.
[63] F. Lucas, D. Tondelier, B. Geffroy, T. Heiser, O. A. Ibraikulov, C. Quinton, C. Brouillac, N. Leclerc, J. Rault-Berthelot, C. Poriel, *Mater. Chem. Front.* **2021**, *5*, 8066–8077.
[64] F. Lucas, C. Brouillac, S. Fall, N. Zimmerman, D. Tondelier, B. Geffroy, N. Leclerc, T. Heiser, C. Lebreton, E. Jacques, C. Quinton, J. Rault-Berthelot, C. Poriel, *Chem. Mater.* **2022**, *34*, 8345–8355.
[65] M. Idris, S. C. Kapper, A. C. Tadle, T. Batagoda, D. S. Muthiah Ravinson, O. Abimbola, P. I. Djurovich, J. Kim, C. Coburn, S. R. Forrest, M. E. Thompson, *Adv. Opt. Mater.* **2021**, *9*, 2001994.
[66] E. Baranoff, B. F. E. Curchod, *Dalton Trans.* **2015**, *44*, 8318–8329.
[67] Y. Xu, Z. Cheng, Z. Li, B. Liang, J. Wang, J. Wei, Z. Zhang, Y. Wang, *Adv. Opt. Mater.* **2020**, *8*, 1902142.
[68] Y. Kondo, K. Yoshiura, S. Kitera, H. Nishi, S. Oda, H. Gotoh, Y. Sasada, M. Yanai, T. Hatakeyama, *Nat. Photonics* **2019**, *13*, 678–682.
[69] S. H. Han, J. H. Jeong, J. W. Yoo, J. Y. Lee, *J. Mater. Chem. C* **2019**, *7*, 3082–3089.
[70] H.-G. Kim, H. Shin, Y. H. Ha, R. Kim, S.-K. Kwon, Y.-H. Kim, J.-J. Kim, *ACS Appl. Mater. Interfaces* **2019**, *11*, 26–30.
[71] X. Song, D. Zhang, Y. Lu, C. Yin, L. Duan, *Adv. Mater.* **2019**, *31*, 1901923.

[72] D. Zhang, X. Song, M. Cai, L. Duan, *Adv. Mater.* **2018**, *30*, 1705250.
[73] B. Madushani, M. Mamada, K. Goushi, H. Katagiri, H. Nakanotani, T. Hatakeyama, C. Adachi, *Adv. Mater.* **2024**, *36*, 2402275.
[74] Y.-T. Lee, C.-Y. Chan, M. Tanaka, M. Mamada, U. Balijapalli, Y. Tsuchiya, H. Nakanotani, T. Hatakeyama, C. Adachi, *Adv. Electron. Mater.* **2021**, *7*, 2001090.
[75] U. Balijapalli, Y.-T. Lee, B. S. B. Karunathilaka, G. Tumen-Ulzii, M. Auffray, Y. Tsuchiya, H. Nakanotani, C. Adachi, *Angew. Chem. Int. Ed.* **2021**, *60*, 19364–19373.
[76] E. Pakhomenko, S. He, R. J. Holmes, *Adv. Opt. Mater.* **2022**, *10*, 2201348.
[77] C. Poriel, J. Rault-Berthelot, *Acc Chem Res* **2018**, *51*, 1818–1830.

Manuscript received: January 22, 2025
Accepted manuscript online: February 26, 2025
Version of record online: March 18, 2025